EFFECTS OF 3D SURFACE TOPOGRAPHY ON REGIONAL AND TELESEISMIC SIGNALS FROM UNDERGROUND EXPLOSIONS

Thorne Lay[1], Megan Avants[1], Xiao-bi Xie[1], and Arthur J. Rodgers[2]

University of California Santa Cruz[1] and Lawrence Livermore National Laboratory[2]

Sponsored by the Air Force Research Laboratory

Award Nos. FA9453-11-C-0234[1] and DE-AC52-07NA27344[2]
Proposal No. BAA11-09

ABSTRACT

Recent underground nuclear tests conducted by North Korea have reaffirmed the importance of near-source rough surface topography for the generation of complex seismic signals observed at regional and teleseismic distances. Complex reflections from the irregular 3D surface scatter into both horizontally and vertically propagating wave fields, producing directionally dependent focusing and defocusing of *P* and *S* wave fields, conversion of *P*-to-*Rg* high frequency energy, and generating complex signal codas, complicating robust event discrimination and precise estimation of burial depth (and hence yield). Quantifying these effects requires numerical methods capable of accurately accounting for the 3D interactions with a rough surface. We are applying two distinct finite difference methods with which we have extensive experience to quantitatively determine the effects of near-source rough topography on seismic waves from shallow underground nuclear explosions, using high-resolution topography models for the North Korea test site and exploring the effects of precise emplacement location relative to the topography. Preliminary work indicates that the very complexity of the wave field that complicates waveform interpretation holds the key to event quantification if the topographic effects are accurately modeled. High-resolution near-source models are being coupled to regional and teleseismic propagators using two methods; representation theorem and embedded slowness array calculations, and comparisons will be made with available recordings from regional arrays and broadband stations and teleseismic IMS arrays. The representation theorem approach has been developed and the LLNL finite difference code WPP has been updated to output strains (from which to compute stresses), as well as displacements, on an integration surface, simplifying the calculation of far-field P wave motions. The goal of this research program is to develop fundamental understanding of the effects of surface topography and guidelines for how resulting waveform complexity can be exploited for precise emplacement location determination, improved yield estimation, and understanding of regional discriminant behavior. We have conducted analysis of regional Lg signals for the 2006 and 2009 North Korean tests. Vertical component broadband seismograms from nine stations were used for the 25 May 2009 event and eight of the same stations for the 9 October 2006 event. An additional 599 broadband seismograms from 82 regional events were used to calibrate the network Lg-magnitudes. The 2009 event is found to have m_b(Lg) = 4.53. The regional Pn velocity is estimated as 8.0 km/s, indicative of stable continental lithosphere, and using a fully-coupled magnitude-yield relation, the yield for the 2009 event is estimated as approximately 2.35 kt.

OBJECTIVES

Seismic waves recorded at regional and teleseismic distances are routinely analyzed to locate, identify and measure the yield of underground nuclear explosions amidst a background of naturally occurring earthquakes. These applications require understanding of elastic wave propagation effects on the seismic waveforms and it is recognized, although incompletely quantified, that the effects of surface topography can be very important for all three applications. Very precise location estimation within a tunneled mountainous terrain is needed to evaluate the effective burial depth beneath any overlying topography. The precision required exceeds that of standard arrival-time location methods, motivating use of complete waveform information, but the roughness of the free surface complicates the nature of depth-phase arrivals (*pP*, *pPn*) in both regional and teleseismic waveforms. Overburden thickness estimates directly influence yield estimation due to predictable effects of confining pressure relative to scaled depth of burial calibration (e.g., Murphy et al., 2010). Enhanced high-frequency S-wave excitation from near-source scattering (*pS*) has strong directionality in radiation, and reduces the discrimination capabilities of regional phases for these events. The relatively strong surface wave excitation may also be influenced by the stress state at the shot point and the topographic environment.

The primary objective of this project involves modeling the effects of 3D rough surface topography on regional and teleseismic signals from shallow underground nuclear explosions. We are performing preliminary 3D work on North Korea, building on the results of Rodgers et al. (2010), and the work on 2D free-surface scattering by He et al. (2008). The overall objectives include:

(1) Verification of the Lawrence Livermore National Laboratory (LLNL) and University of California, Santa Cruz (UCSC) 3D finite difference codes using the North Korea surface topography model with various degrees of smoothing. This is important for recognizing the stability and reproducibility of results for different formulations of the numerical solution for a rough free surface.

(2) For both WPP and the UCSC code, implement both the 2D and 3D finite-difference simulation and local slowness analysis (FDSA) methods of Xie et al. (2005) and Xie et al. (2007) along with connection to teleseismic propagators using the representation theorem. For WPP the FDSA method is directly useful, as the solution produces the displacement field directly, and we will process embedded arrays to separate energy with varying slowness and slant-stack to generate specific teleseismic *P* wave synthetics. For the representation theorem, stress vectors and displacements are computed over a bounding surface in the lower portion of the finite-difference grid and integrated to provide a far-field response using appropriate teleseismic point-force and point-couple Green functions.

(3) Implement connection to regional phases synthetics for both WPP and the UCSC code. FDSA is already configured for the UCSC finite difference code for regional phases, and we can couple this to either mode or frequency-wavenumber propagators. This effort is essential to go from near-field complete wave fields which are informative, but not directly observed, to isolated regional distances where signals are observed.

(4) Using both codes, extend the modeling of sensitivity to surface roughness, position of the source relative to the scattering topography, and observability of the effects at regional and teleseismic distances. Consider several near-source topographic environments to understand S wave generation, Rg-to-P scattering, and pP effects.

(5) By comparison of synthetics and data, we will seek to refine the location and depth of events. The analysis of sensitivity to position above will be exploited to determine which aspects of the complex wave field provide information about the source position, depth beneath the surface, and explosion yield. The best data for comparison is certainly the regional broadband recordings for North Korea, along with stacked signals from IMS arrays at teleseismic distances.

RESEARCH ACCOMPLISHED

We performed a series of numerical simulations of shallow explosions to investigate the effect of surface topography on ground motions with particular emphasis on scattering and the generation of shear waves. Seismic wave simulations were performed with the WPP anelastic finite difference code developed at LLNL (Petersson, 2010). This code uses an algorithm based on a second-order node-centered finite difference scheme (Nilsson et al., 2007; Petersson and Sjogreen, 2010) including free-surface topography using a curvilinear grid (Appelo and Petersson, 2008). Simulations represented a Cartesian domain 30 km x 30 km x 15 km with a grid spacing of 25 m. We used material properties representative of seismically fast granitic rock (5190 m/s, 3000 m/s and 2500 kg/m^3 for the P- and S-wave wavespeeds and density, respectively). The second order WPP method requires 15 points per wavelength for numerical accuracy, so the calculations were accurate to frequency up to 8 Hz. The calculations were run out to about 12 seconds after the origin time and required nearly one billion (1x10^9) grid points. No anelastic attenuation was included in these calculations in order to isolate elastic scattering effects.

Surface topography was generated by the Fourier method with random phase (Frankel and Clayton, 1986). The correlation structure was chosen to be a von Karman function with an isotropic correlation length of 2000 m. The mean elevation of the topography was set to 1000 m and the standard deviation was varied from 50 m to 300 m. Topographic variations were kept limited to a threshold of plus or minus three standard deviations, so that topography varied by ±150 m to ±900 m, for standard deviations of 50 and 300 m, respectively. Figure 1a shows the topography for one realization. The source was placed at the center of the domain at a depth of 500 m below the surface. Three-component ground motion time-series were output along profiles (every 15° in azimuth) radiating from the source from 5-30 km, with 1 km spacing. Figure 1a also shows the points on the surface where ground motion time-series were recorded.

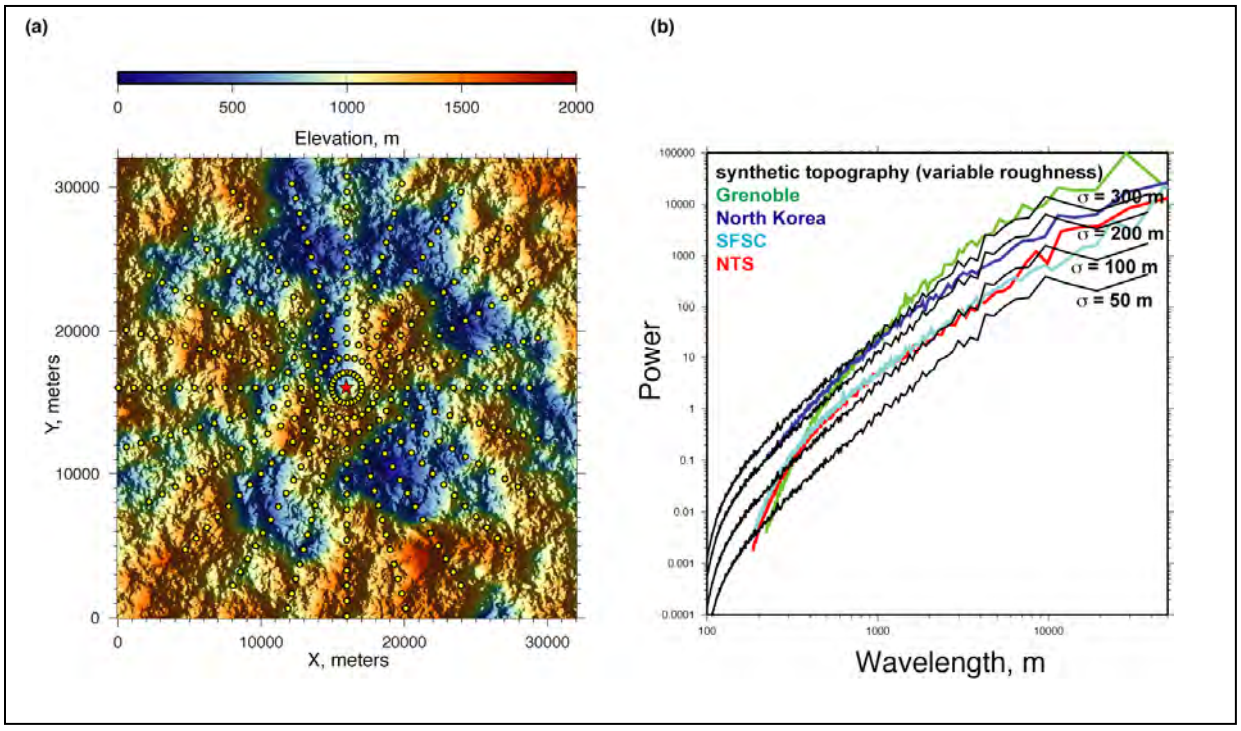

Figure 1. (a, left) Computational domain showing randomly generated surface topography (color scale), source (star) and marker points where ground motions were output (yellow triangles). (b) Power spectra of surface topography as a function of wavelength for (black) the random topography generated with the von Karman autocorrelation function (correlation length of 2000 m and standard deviations of 50, 100, 200 & 300 m). Also shown are the power spectra of actual topography for four regions: Grenoble Basin (green); North Korean nuclear test site (blue); Nevada Test site (red); and San Francisco Bay Area (cyan).

Surface topography is represented in WPP with a curvilinear mesh. The actual topography is read into the code and spatially filtered based on the gird spacing at the surface and wave propagation parameters so that no short wavelength waves will be introduced by interaction with the surface. For sufficiently small grid spacing and/or smooth topography the curvilinear mesh honors the topography. We used a von Karman autocorrelation function to generate the random topography and this has power at short wavelengths. Some of the topographic power is reduced after WPP spatially filters the surface in order to render it on the computational mesh; however, for the fast wavespeeds and fine mesh (25 m) this has only a modest effect on the surface roughness for wavelengths less than 500 m (on the order of the wavelength of highest frequencies resolved on the mesh).

The correlation structure of the topography was chosen because it matches closely that of actual topography. Figure 1b shows the topographic power versus wavelength for four regions (colored lines) of comparable domain size to our simulations: Grenoble, France (in the French Alpes, studied by Chaljub et al., 2010); North Korea (studied in Rodgers et al., 2010); San Francisco Bay, Santa Clara Valley and East Bay Hill; and the Nevada National Security Site (formerly the Nevada Test Site), southern Nevada. Note that in the range of wavelengths from 500–20000 m the actual topographies have a very similar slope, but are offset by different roughnesses or multiplicative factors. By trial and error we found that these topographic correlation structures can be well matched by a von Karman autocorrelation function with correlation length of 2000 m. The synthetic topographies were generated by the Fourier method and their powers are shown with black with the range of topographic roughness: 50, 100, 200 and 300 m. These match the correlation structure of a range of actual topographies and indicates that the assumed correlation structure for the free surface is representative of regions of the Earth with rough topography.

Simulations of ground motions for shallow explosions in a homogeneous half-space show that free surface topography very strongly alters the wavefield. Figure 2 shows the vertical component ground motions in record section format for two of the topographic realizations with different roughnesses: 50 m for (a) and 200 m for (b). The motions at all 24 locations at the same distance from the event along each of the radial lines are plotted in gray and the mean response (stack of all traces at a given distance) is shown in red. In this plot the seismograms are scaled by the square-root of distance so that the surface wave (Rg) should have constant amplitude, reflecting only geometric spreading. Note that the variability in the P-wave amplitudes and waveforms is quite small, however the variability between individual traces increases with time in the window between P and Rg, due to P-to-S scattering. Furthermore, note that the amplitude of scattered energy is proportional to the topographic roughness.

In order to quantify the effect of topographic scattering on high-frequency ground motions near explosions we windowed the phases and measured the Fourier amplitude spectra of each phase. Figure 3a shows the response at 10 km range for a single azimuth for the flat case (which corresponds to a half-space response) and the topographic case with a roughness of 100 m. The response varies with azimuth for the topographic case, but not for the flat case. Note that the P, P-coda and Rg phases are windowed and indicated by the different colors. The Fourier amplitude spectra are computed for each window and shown in Figure 3b. Note that the P spectra for the flat case is broadband, representing the source spectrum, while the Rg spectrum for the flat case is peaked due to the excitation eigenfunction of the fundamental mode Rayleigh wave. The P-coda has no energy for the flat case. For the topographic case the P spectra is broadly similar to that of the flat case, with some modulation due to scattering. The P-coda spectrum for the topographic case is non-zero and tracks the P spectrum with amplitude about a factor of three less than the P spectrum. The Rg spectrum for the topographic case has the same peak frequency as the flat case (1-2 Hz), but does not decay rapidly as it does for the flat case. Energy in the Rg window for the topographic cases roughly tracks with the P spectrum and is up to a factor of ten greater than that for the flat case.

The individual spectra for the P, P-coda and Rg windows show substantial path-specific variability. However, if the spectra for traces recorded at 10 km range and each topographic roughness are grouped together ensemble behavior emerges. Figure 3c shows the average spectra for the flat and four topographic roughnesses. Remarkably, the P spectra are not impacted by the different roughnesses, but the P-coda and Rg spectra show a strong dependence on topographic roughness. As the surface roughens, the P-coda spectra are uniformly increased, approaching the P spectra and mimicking the source spectrum. The Rg spectra for the topographic cases maintain the peak frequency of 1-2 Hz characteristic of the flat (half-space) solution, but as the topography roughens the Rg window contains more and more higher frequency energy.

These results indicate that scattering of P-to-Rg by surface topography is efficient at generating high frequency energy in the S-wave window. How this energy propagates to long range is a question we hope to investigate. Key

to our investigations will be to evaluate the vector slowness of energy in the Rg window near the source (< 10 km). We will investigate the composition of this energy (P- or S-wave), whether it is trapped in the crust or escapes to the

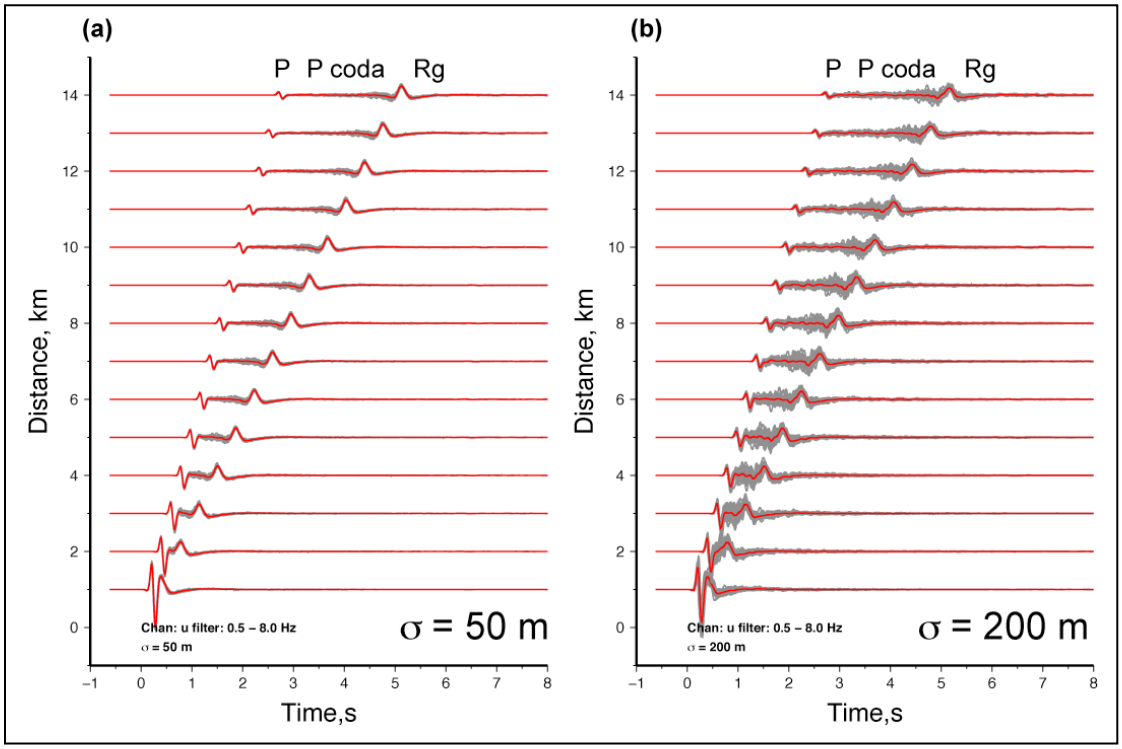

Figure 2. Record section of vertical component ground motions for two realizations of surface topography with different topographic roughness of (a) 50 m and (b) 200 m. The individual traces at each marker point from the domain map (Figure 1a) are shown in gray and the mean response at each distance is shown in red.

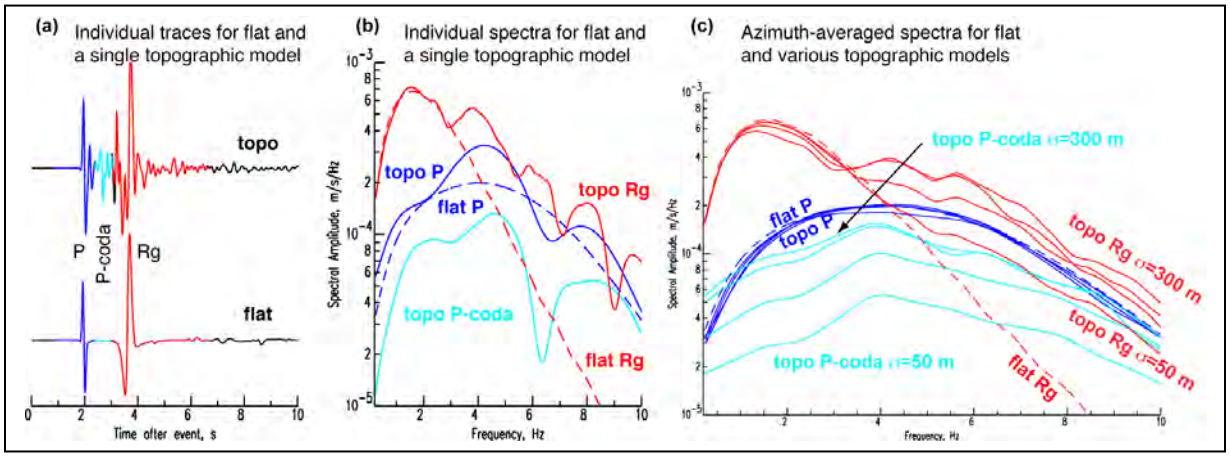

Figure 3. (a) Vertical component traces at 10 km for a single topographic (top) and the flat (bottom) case. The P, P-coda and Rg windows are indicated by the blue, cyan and red colors, respectively. (b) The Fourier amplitude spectra for a single topographic (solid) and the flat (dashed) case using the windowed traces shown in (a) and using the same color scheme. (c) Average spectra at 10 km for all azimuths for various topographic roughnesses (solid) and the flat case (dashed).

mantle and with what horizontal slowness. Note that we observe substantial energy on the transverse component in these simulations as was shown in Rodgers et al. (2010). The generation and fate of this energy will also be investigated.

The near-source computations can be performed with the 3D finite-difference algorithm as shown above; however, connection to observations requires prediction of far-field waveforms or spectral measures at both regional and remote locations. This requires coupling of the finite-difference calculations to long-range propagators in one form or another, and we are using two approaches; wavefield decomposition into energy partitioned by wave slowness and representation theorem coupling to far-field Green functions. In our initial work, coupling from the WPP grid to far-field is being performed by integration over a deep horizontal surface within the WPP grid, far enough removed from the absorbing boundary condition domain that the down-going signals are accurately retained. The representation theorem involves integration of the displacements and tractions acting on a surface enclosing the source domain contracted with corresponding point couple and point source Green function responses, respectively.

Figure 4 illustrates computation of the necessary displacement and stress component terms on a deep horizontal surface of the WPP grid below a surface vertical point-force calculation. WPP directly computes displacements, and we initially used the 3D displacement field to compute the necessary traction-vector components. As with any

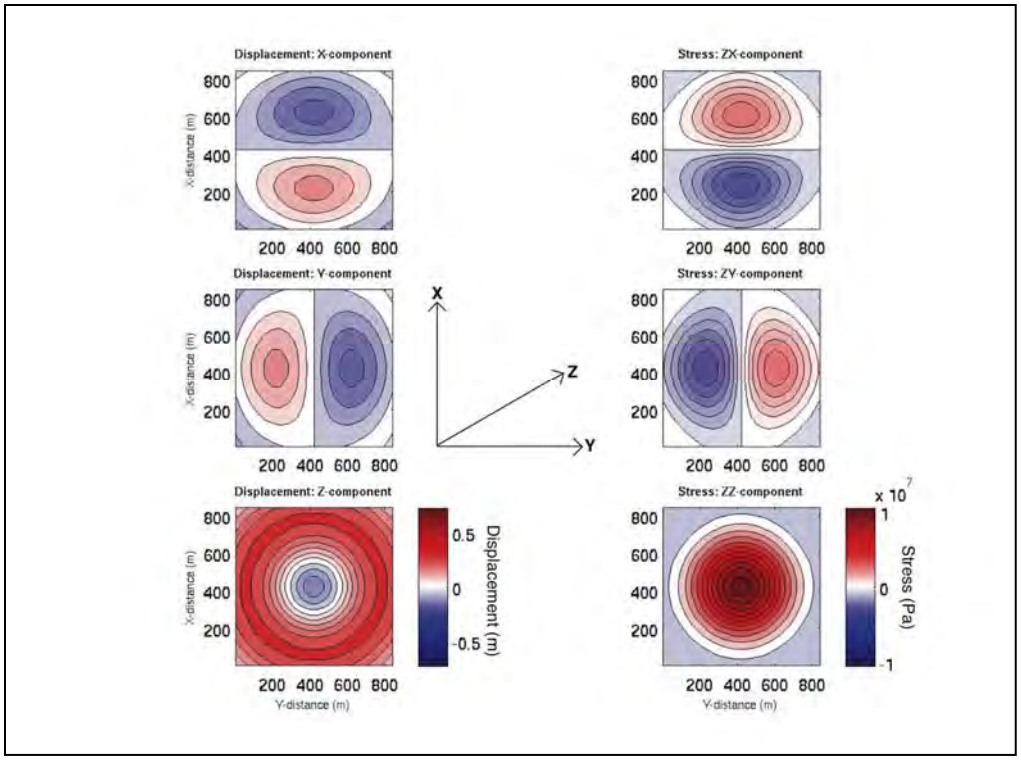

Figure 4. A snapshot of the movie of displacement and stress components on a horizontal plane near the bottom of the 3-D WPP computational domain. Shown in the left column from top to bottom are the x-, y-, and z-components of displacement recorded at each grid point across the plane. The right column contains the x-, y-, and z-components of stress acting on this plane. The seismic source for this example is a point force acting straight down (into the plane of the figure) on the surface of the 3-D computational domain, and is located directly above the center of each plot as shown. The grid origin is in the lower left corner. The z-components of displacement and stress are most intuitive—the initial positive displacement (red) in the z-direction is expanding across the plane, and the stress magnitude is greatest near the center of the grid which is where the z-component of displacement has transitioned from from positive (downward) to negative (upward).

surface integral technique, the main considerations include smoothness of the fields over the surface, accuracy of the integration and suppression of integral truncation effects. During this year's research WPP was modified by LLNL

to output strain calculations directly so that we could eliminate the step of writing out multiple grid layers of displacement time histories for computing stresses using difference operators. We have compared the predictions of stress terms from the strains directly and from our earlier difference calculations and found excellent agreement, so the new output capabilities will greatly facilitate applications of the representation theorem to WPP calculations. With six output time series indicated in Figure 4, we predict a far-field response using travel time variations across the integration surface along with radiation pattern terms for single force and couple terms activated by the stress and displacement fields, respectively. The integrated contribution from each stress vector term and each displacement term (with the latter being time-differentiated due to the spatial derivative of the Green function operator that weights them), is then summed to make the far-field synthetic waveform. Much of the effort this year has addressed stabilizing the integration to the intrinsic truncation of the edges of the integration surface and dealing with suppression of near-source energy such as down-going S wave energy from the source (for double-couple sources), which can produce strong arrivals that sweep across the integration surface that are not of interest. Currently this is being done with simple ray theory (geometric spreading, with a constant ray parameter calculation of the receiver function using a propagator matrix), and we are exploring sensitivity to the very small variations of ray slowness across the grid and the subtle effects of embedding the Cartesian grid into a spherical model.

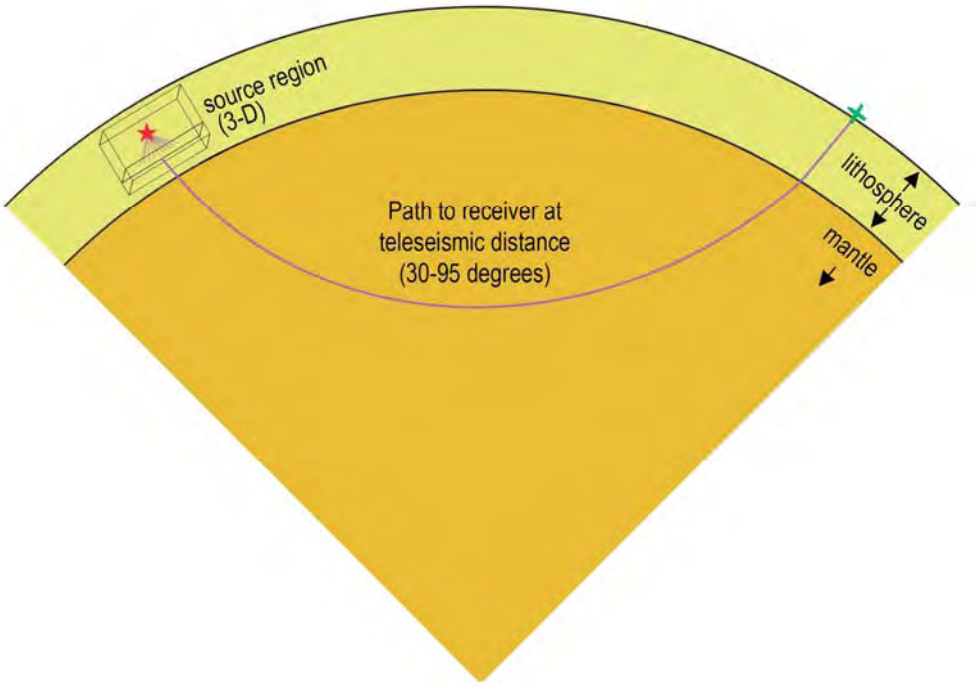

Figure 5. Teleseismic propagation of the stress and displacement wave excitation on the lower surface of the near-field finite-difference grid to the far-field. We are using ray theory to make the far field synthetic seismograms from the surface integrated responses.

As part of our analysis of the North Korean test site effects, we have been examining the regional phases for the underground tests and exploring their implications for the explosion yields. We have just published a paper (Zhao et al., 2012), in which we have describe analysis of the regional Lg signals for the 2006 and 2009 North Korean tests. Vertical component broadband seismograms from nine stations (Figure 6) were used for the 25 May 2009 event and eight of the same stations were used for the 9 October 2006 event (Zhao et al., 2008). An additional 599 broadband seismograms from 82 regional events were used to calibrate the network Lg-magnitudes. The 2009 event is found to have $m_b(Lg)$ = 4.53. The regional Pn velocity is estimated as 8.0 km/s, indicative of stable continental lithosphere, and using a fully-coupled magnitude-yield relation, the yield for the 2009 event is estimated as approximately
2.35 kt. The regional Q model has strong path variations, complicating separation of source and path effects on the

Lg signals (Figure 7). Our expectation is that the regional Pn and teleseismic P signals will provide the best control on the topographic contributions.

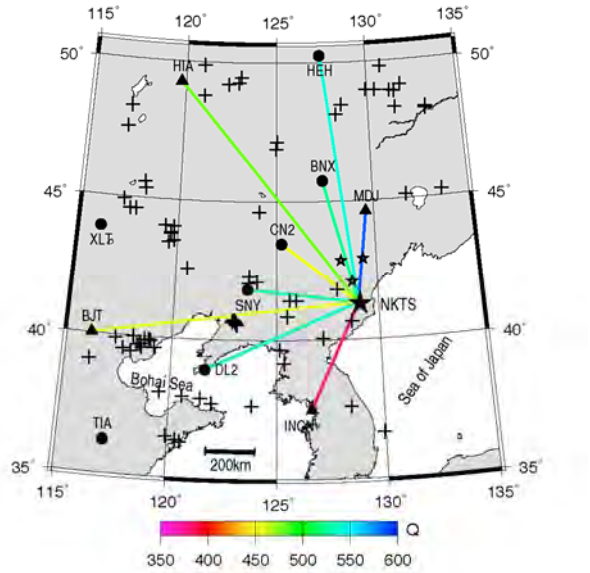

Figure 6. Map showing the locations of the North Korea test site (solid star labeled by NKTS) and CNDSN (solid circles) and GSN (triangles) stations used in this study. Also illustrated in the figure are epicenters of earthquakes (crosses) which occurred between December 1995 and May 2009 and three small chemical explosions (hollow stars) with known yields. The colors on great circle ray paths from the NKTS to individual stations denote the average path Q extracted from the Lg wave Q model. The Q values vary between 379 and 589. (From Zhao et al., 2012).

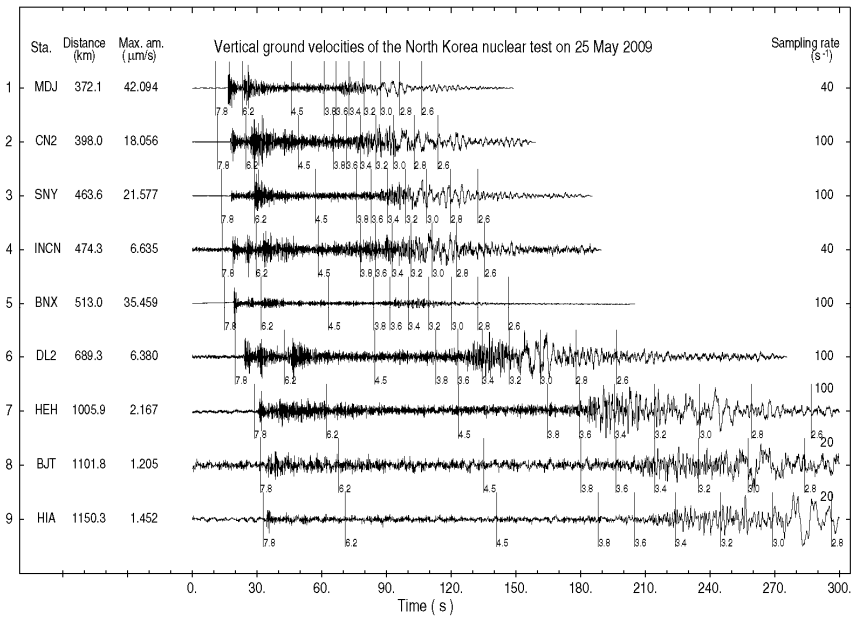

Figure 7. Vertical ground velocities observed from the May 25, 2009 North Korea nuclear explosion. The traces are ordered according to their epicentral distances. The station names and peak amplitudes in μm/s are listed on the left side, and the corresponding sampling rates are listed on the right side.

Vertical bars and numbers on the traces indicate apparent group velocities. (From Zhao et al., 2012).

CONCLUSIONS AND RECOMMENDATIONS

At this phase of work on this project, we have established the strong impact of surface scattering on the near-source wavefield using realistic realization of free-surface topography. Modulation and enhancement of short-period signals and generation of scattered coda can be significant, and these effects can impact far-field measurements. Progress has been made on connecting the near-source finite-difference environments to the far-field using the Representation Theorem. We are beginning comparisons with the effects of slowness analysis from and embedded three-dimensional grid of displacement calculations; as this provides an independent approach to capturing the finite-frequency contributions to the far-field displacements. We have performed analysis of the large regional data set for eastern China, including good quality Lg observations for the 2006 and 2009 North Korean tests. The $m_b(Lg)$ value for the 2009 event is 4.53.

REFERENCES

Appelo, D., and N. A. Petersson (2008). A stable finite difference method for the elastic wave equation on complex geometries with free surfaces, *Comm. Comput. Phys*. **5**, 84–107.

Chaljub, E., P. Moczo, S. Tsuno, P.-Y. Bard, J. Kristek, M. Käser, M. Stupazzini, and M. Kristekova (2010). Quantitative Comparison of Four Numerical Predictions of 3D Ground Motion in the Grenoble Valley, France, *Bull. Seismol. Soc. Am*. **100**, 1427–1455, doi: 10.1785/0120090052.

Frankel, A., and R. Clayton (1986). Finite Difference Simulations of Seismic Scattering: Implications for the Propagation of Short-Period Seismic Waves in the Crust and Models of Crustal Heterogeneity, *J. Geophys. Res*. **91** (B6), 6465–6489.

He, Y., X.-B. Xie, and T. Lay (2008). Explosion-Source Energy Partitioning and *Lg*-Wave Excitation: Contributions of Free-Surface Scattering, *Bull. Seismol. Soc. Am*. **98**, 778–792.

Murphy, J. R., B. C. Kohl, J. L. Stevens, T. J. Bennett, and H. G. Israelsson (2010). Exploitation of the IMS and other data for a comprehensive advanced analysis of the North Korean nuclear tests, SAIC Final Technical Report. DOS Contract No. SAWMMA09C0250.

Nilsson, S., N.A. Petersson, B. Sjogreen, H.-O. Kreiss (2007). Stable difference approximations for the elastic wave equation in second order formulation, *SIAM J. Numer. Anal*. **45,** 1902–1936.

Petersson, N. A. (2010). https://computation.llnl.gov/casc/serpentine/software.html (website).

Petersson, N. A., and B. Sjögreen (2010). Stable grid refinement and singular source discretiztion for seismic wave simulations, LLNL-JRNL-419382, *Communications in Computational Physics*.

Rodgers, A. J., N. A. Petersson, and B. Sjogreen (2010). Efficient generation of shear waves from shallow explosions by topographic scattering near the North Korean nuclear test site, *J. Geophys. Res*., doi:10.1029/2010JB007707, LLNL-JRNL-433892.

Xie, X. B., Z. Ge, and T. Lay (2005). Investigating explosion source energy partitioning and Lg-wave excitation using a finite-difference plus slowness analysis method, *Bull. Seismol. Soc. Am*. **95,** 2412–2427.

Xie, X. B., T. Lay, R. S. Wu, and Y. He (2007). Near source energy partitioning for regional waves in 2d and 3d models, effects from random free surface scattering, in *Proceedings of the 29th Monitoring Research Review: Ground-based Nuclear Explosion Monitoring Technologies*, LA-UR-07-5613, Vol. 1, pp. 322–332.

Zhao, L.-F., X.-B. Xie, W.-M. Wang, and Z.-X. Yao (2012). Yield estimation of the 25 May 2009 North Korean Nuclear explosion, *Bull. Seism. Soc. Am*. **102**, 467–478, doi:10.1785/0120110163.

Zhao, L. F., X. B. Xie, W. M. Wang, and Z. X. Yao (2008). Regional seismic characteristics of the 9 October 2006 North Korean nuclear test, *Bull. Seism. Soc. Am.* **98,** 2,571–2,589, doi: 10.1785/0120080128.